

INPC: Implicit Neural Point Clouds for Radiance Field Rendering

Florian Hahlbohm¹, Linus Franke², Moritz Kappel¹, Susana Castillo¹,
Marc Stamminger², and Marcus Magnor¹

¹ Computer Graphics Lab, TU Braunschweig, Germany
{lastname}@cg.cs.tu-bs.de

² Visual Computing Erlangen, FAU Erlangen-Nürnberg, Germany
{firstname.lastname}@fau.de

<https://fhahlbohm.github.io/inpc/>

Abstract. We introduce a new approach for reconstruction and novel-view synthesis of unbounded real-world scenes. In contrast to previous methods using either volumetric fields, grid-based models, or discrete point cloud proxies, we propose a hybrid scene representation, which implicitly encodes a point cloud in a continuous octree-based probability field and a multi-resolution hash grid. In doing so, we combine the benefits of both worlds by retaining favorable behavior during optimization: Our novel implicit point cloud representation and differentiable bilinear rasterizer enable fast rendering while preserving fine geometric detail without depending on initial priors like structure-from-motion point clouds. Our method achieves state-of-the-art image quality on several common benchmark datasets. Furthermore, we achieve fast inference at interactive frame rates, and can extract explicit point clouds to further enhance performance.

Keywords: novel-view synthesis · point clouds · implicit representations

1 Introduction

Novel-view synthesis describes the task of rendering novel inter- or extrapolated views from a set of input images, which is an inherently difficult problem. Recent methods commonly address this by reconstructing the scene either volumetrically as dense implicit radiance fields [38] or use explicit geometric representations [50] such as point clouds or meshes. Leveraging advances in optimization-based neural rendering techniques, volumetric approaches achieve an impressive increase in quality by optimizing geometric information (i.e., density and appearance) into *Multi-Layer Perceptrons (MLPs)* [34], voxel grids [18], or hash maps [36]. In contrast, explicit point-based methods optimize appearance at discrete 3D scene points, where color is being represented via 3D Gaussians [27] or per-point features [1]. While both directions provide unique advantages, they also entail severe drawbacks such as volumetric methods relying on intensive ray-marching or explicit methods requiring a-priori point proxies.

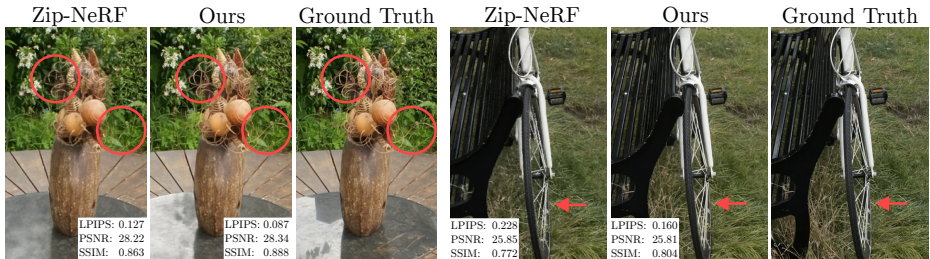


Fig. 1: Our implicit point cloud optimization and rendering excels at capturing small details. It renders sharply and a magnitude faster than the current state of the art Zip-NeRF. The shown metrics are averages over the full test set of the respective scene.

In this work, we aim at creating a novel efficient and robust scene representation which combines the benefits of both worlds while bypassing the need for expensive ray-casting or explicit priors. To this end, we introduce Implicit Neural Point Cloud (INPC), an implicit volumetric scene representation that enables accurate scene reconstruction by sampling and subsequent rendering of explicit point clouds using fast differentiable rasterization. More specifically, we take inspiration from current state-of-the-art approaches 3D Gaussian Splatting [27] and Zip-NeRF [5]: We decompose and optimize a scene into two parts, which constitutes a concept that we dub *implicit point cloud*. Here, the geometric structure is represented as an octree-based point probability field, while appearance features are embedded in an *implicit* coordinate-based multi-resolution hash grid. The octree is progressively subdivided to ensure similar probability distribution across all leaf nodes, which enables the reconstruction of fine articulated geometry while optimizing the capacity of our appearance hash grid. During rendering, we use the probability octree as an estimator for point positions and use either random positions in each leaf or fixed sampling patterns, while per-point appearance features are queried from the hash grid. The resulting *explicit* point cloud is then rendered via fast bilinear splatting, where gradients are backpropagated through our fully differentiable end-to-end pipeline to the implicit representation. By combining the advantages of both families of approaches, our method achieves robust radiance field reconstruction alongside rendering with state-of-the-art quality on commonly used datasets, as seen in Fig. 1. In summary, our contributions are:

- The introduction of implicit point clouds as a data structure to effectively capture and optimize unbounded 3D scenes.
- An algorithm for extracting view-specific point clouds as well as global point clouds from this model.
- A fast and differentiable rendering formulation for this data structure using bilinearly splatted points.

2 Related Work

Traditionally, novel-view synthesis was based on light fields [20], however image-based rendering became a popular alternative [50]. It commonly works by warping source views onto geometric proxies [6, 12]. This proxy may contain artifacts, especially near object edges, either due to limited input coverage or misaligned cameras. With image-based rendering, these artifacts result in blurred and inaccurate images, with subsequent methods lessening these artifacts [6, 15]. The geometric proxy can also be a full 3D reconstruction, which with the introduction of *Structure-from-Motion (SfM)* [45] and *Multi-view Stereo (MVS)* [49] gained popularity. Furthermore, the advent of deep learning-based techniques in this field further improved results [52] through learned blending operators [24] and textures [53], lessening failure cases introduced by artifacts in the reconstruction. In the following, we discuss related works in volume- and point-based novel-view synthesis, the two directions we combine in our work.

Neural Radiance Fields. Recently, implicitly representing 3D scenes within volumetric fields became popular, enabling novel-view synthesis via volume rendering and distancing themselves from proxy geometry. Mildenhall *et al.* [34] showed exceptional results by compressing a complete 3D scene into a large coordinate-based MLP, a concept called *Neural Radiance Field (NeRF)*. To render images, pixel-wise ray-marching is used with the volume rendering formulation for each pixel color C :

$$C = \sum_{i=1}^N T_i \alpha_i \mathbf{c}_i \quad \text{and} \quad T_i = \prod_{j=1}^{i-1} (1 - \alpha_j), \quad (1)$$

with

$$\alpha_i = (1 - \exp(-\sigma_i \delta_i)).$$

Here, densities σ and color \mathbf{c} are the outputs of the MLP at each ray interval δ_i . Several successive works aim to resolve challenges bound to this concept by addressing input view distributions [11, 30, 65], memory usage [41], and computation times [3, 8, 11, 36, 37, 51, 54]. For the latter, discretizing the scene space using voxel grids [18], octrees [44, 64], tensor decomposition [7], or even distilling a faster model for inference with neurally textured triangle meshes [9] or mesh baking [14, 62] proved effective. In terms of training and rendering speed, *Instant-NGP* [36] presented exceptional results with a hash grid-based space partitioning scheme, allowing training within minutes and framerates of up to 10 fps. Furthermore, close to our approach are hybrids of conventional and optimized ideas: Point-NeRF [60] uses an explicit point cloud with neural features, however images are rendered with slow ray-marching and they are restricted to reconstruct bounded scenes. Regarding quality, Barron *et al.* propose anti-aliasing through conical frustum sampling [3] and enable extension to unbounded scenes via space contraction [4]. The current state-of-the-art in this field, *Zip-NeRF* [5], combines ideas from both quality and efficiency directions: It augments the underlying grid-based data structure with anti-aliasing through conical sampling, the addition

of scaling information, and refined empty space skipping. While Zip-NeRF is comparably fast in training (taking about 5 hours), the rendering speed for novel views is limited to ~ 0.2 fps on consumer-grade hardware. This approach is closest in mind to our method, as we also recombine grid-based appearance information with implicit density formulation for scene reconstruction. In contrast to Zip-NeRF, however, our method enables rasterization-based rendering, making it faster in inference.

Point Rendering. Orthogonal to NeRFs, neurally rendering radiance fields via explicit points is an established and efficient methodology for novel-view synthesis. Early work builds on established techniques [25] and associates point clouds obtained through MVS with optimizable colors or features [1]. Points are rendered as splats of varying sizes and a large *convolutional neural network (CNN)* is used to interpret features. Due to the unstructured and disconnected nature of point clouds, holes in image space where no point was projected to can appear, which the neural network can also fix. Several follow-up works have been proposed eliminating training time [23, 39], adding per-view feature optimization [32], reflection warp-fields [31], or differentiable tone mapping [43]. Furthermore, differentiability w.r.t. point positions and camera parameters – via approximate [43] or linear gradients [17] – has been introduced, retaining rendering performance for large point clouds compared to other point representations [33, 58, 63]. Recent point-based radiance field renderers [16, 17, 27, 31, 32, 63] also adapt NeRFs rendering technique to α -blending points. Instead of taking N samples along a ray as in Eq. (1), they blend together \mathcal{N} sorted points with associated colors c and opacities α instead of computing α based on density. For approaches keeping true to the MVS reconstruction, the concurrent work *Trilinear Point Splatting (TRIPS)* [17] is most similar to our point rendering, as it also uses bilinear point splatting followed by a neural network for feature decoding. However its reconstruction quality is limited by the quality of the MVS reconstruction, as no point cloud augmentations are performed.

Overcoming the reliance on point cloud priors has been proposed in several ways. Recent improvements to MVS algorithms via CNNs [55, 61] as well as leveraging NeRFs [57] or transformers [13, 56] lessened the problem, while recent approaches also included the point cloud optimization process directly into the radiance field rendering pipeline. This is done either with additional points via error propagation [67], 3D error volumes [16], point growing via density estimation [60], or gradient-based densifications [27]. Especially important here is *3D Gaussian Splatting (3DGS)* [27] which extends point rendering with anisotropic 3D Gaussians as a radiance field rendering paradigm. Apart from removing the need for a CNN to fill holes, this formulation allows them to start with a sparser point cloud that is densified by repeatedly splitting large Gaussians during the optimization.

In contrast, our approach captures more fine details, as we are able to optimize and render more detailed geometric and appearance information in our implicit point cloud. Furthermore, we are independent from an initial point cloud, thus increasing robustness.

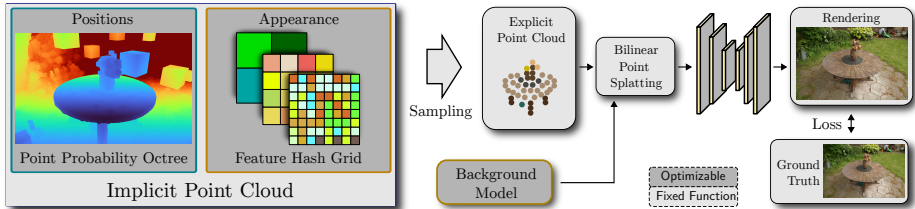


Fig. 2: Overview of our method: We introduce the implicit point cloud, a combination of a point probability field stored in an octree and implicitly stored appearance features. To render an image for a given viewpoint, we sample the representation by estimating point positions and querying the multi-resolution hash grid for per-point features. This explicit point cloud, together with a small background MLP is then rendered with a bilinear point splatting module and processed by a CNN. During optimization, the neural networks as well as the implicit point cloud are optimized, efficiently reconstructing the scene.

3 Method

A minimal point cloud capable of novel-view synthesis, is described by multiple data points consisting of a 3D position vector as well as color information, either through explicit RGB colors or decodable neural features. In our method, instead of storing these spatial and photometric properties in the same data-structure, we split them and optimize both implicitly: Positions as an octree-based probability field \mathcal{P} and appearance, *i.e.* colors/features and opacity, as a neural field \mathcal{A} . These two parts combined constitute what we call an *implicit point cloud*.

Input to our method is a collection of posed RGB images as well as an estimated bounding box. From this, we initialize \mathcal{P} as a voxel-based structure, which our algorithm iteratively refines into an octree to store probabilities for geometry (Sec. 3.1). This structure is then used as an estimator for point positions (Sec. 3.2). These positions are fed into \mathcal{A} – for which we use a multi-resolution hash grid [36] – to retrieve opacity and spherical harmonics (SH) appearance features (Sec. 3.3). These parts are core to our proposed implicit point cloud structure, as they allow us to optimize a radiance field efficiently, with fine geometric granularity and great detail.

An overview of our method is depicted in Fig. 2. It works as follows: First, for a given viewpoint we sample the implicit point cloud, as described above. The resulting explicit point cloud, *i.e.* positions and associated features, is then processed first by rasterizing with a bilinear point splatting (Sec. 3.4) into multi-resolution 2D feature maps [1, 43], then α -blended with the output of a background model, and lastly post-processed by a rendering network with a U-Net architecture [42] (Sec. 3.5). During training, all parts are optimized end-to-end with specifically crafted loss and regularizers (Sec. 3.6). We proceed by describing all components in detail.

3.1 Sparse Point Probability Octree

Existing NeRF methods do not require explicit geometry as they place point samples along per-pixel camera rays [34]. In contrast, point-based methods require a persistent set of explicit point positions during the optimization.

One goal of this work is removing the need for a persistent set of point positions within a typical point-based neural rendering pipeline. Regular occupancy grids have proven to be a useful tool for skipping empty space [19, 36], however, the fixed voxel size used makes it difficult to accurately model complex geometry. To this end, we propose to use a sparse octree storing point probabilities p_i for each leaf node. During the optimization, nodes are updated, subdivided, or pruned depending on their current probability. This allows for accurate reconstruction of fine geometric structures. By then sampling the implied multinomial distribution, we can use these probabilities to sample a point cloud on demand (Sec. 3.2).

Initialization. We initialize the probability field with a uniform 3D voxel grid as the initial leaf nodes of the sparse octree with probabilities set to one. Optionally, we can incorporate a point cloud \mathcal{I} as a prior. Assuming $|\mathcal{I}_i|$ is the number of points inside the volume of the i -th leaf node and Q is the 0.95-th quantile of these point counts, we compute the initial probability as

$$p_i = \min(1.0, \max(0.1, \frac{|\mathcal{I}_i|}{Q})). \quad (2)$$

Probability Updates. The probability of each leaf node should represent how much of its volume is occupied by geometry *relative to other leaf nodes*. To this end, we employ an updating strategy that combines exponential decay and knowledge from the current 3D model, inspired by Müller *et al.* [36]. During optimization, we update the probabilities of all leaf nodes after each optimization step (p'_i) using the following formula:

$$p'_i = \max(\lambda_u \cdot p_i, \max(\{b_0, \dots, b_n\})), \quad (3)$$

where $\{b_0, \dots, b_n\}$ is the set of α -blending weights (p_i) of all points generated using the i -th leaf node. We use $\lambda_u = 0.9968$, in contrast to Müller *et al.*, to account for us updating every iteration. Additionally, we use the transmitted blending weight $b_j = \alpha_j T_j$ (Eq. (1)) for the updates. This imposes a visibility prior on the probabilities, as partially hidden points receive less transmittance. To ensure a stable optimization, we perform no updates in the first 100 iterations, as \mathcal{A} does not contain reliable information yet.

Subdivision. Our updating strategy causes leaf nodes whose volume is only partially filled with geometry to receive a large probability through the max operator in Eq. (3). Thus, it is sufficient to keep the condition for subdivision of a leaf node simple and subdivide all leaf nodes that have a probability above a threshold τ_s . We use $\tau_s = 0.5$ to subdivide every 500 iterations during the optimization and have created leaves inherit their parents' probability.

Due to limitations of efficient multinomial sampling with respect to numerical precision, we only subdivide if the resulting number of leaves is less than 256^3 .

Pruning. By repeatedly applying Eq. (3), the probability of leaf nodes whose volume is empty will exponentially decay towards zero, as such we remove leaf nodes whose probability is less than $\tau_p = 0.01$ every 100 iterations. To prevent failure cases, we only start pruning after the first 500 iterations.

3.2 Point Sampling Strategies

Central to this work is the idea of sampling high-quality point clouds using the implicit octree-based point position estimator introduced in Sec. 3.1. Especially during the optimization, we face the common issue of being limited in terms of GPU memory and are therefore restricted to a fixed budget for the number of sampled points.

This leads us to design two sampling strategies: A viewpoint-specific and a viewpoint-independent sampling scheme. For training, we want to generate a point cloud to render a specific viewpoint with which we can then compute the loss function in each iteration. In contrast, a global, viewpoint-independent point cloud increases temporal stability as well as rendering performance, as no per-frame sampling of the implicit point cloud is required. In the following, we detail the considerations that went into designing both sampling strategies.

Viewpoint-Specific Sampling. We identify three key properties of an effective re-weighting scheme for a specific viewpoint: (1) No samples should be placed outside of the view frustum, (2) regions further away from the camera require less samples, and (3) leaves with a higher subdivision level l , *i.e.*, those representing a smaller volume, should be sampled less. Specifically, we compute the viewpoint-specific probability \hat{p}_i as follows:

$$\hat{p}_i = \mathbb{1}_{visible} \cdot \frac{p_i}{d_i \cdot 2^{l_i \cdot \lambda_l}}, \quad (4)$$

where $\mathbb{1}_{visible}$ is an indicator function returning one for visible leaves and zero otherwise, λ_l weighs down how much a smaller voxel should be sampled, and d_i represents the distance between leaf center and the image plane. Empirically, we found $\lambda_l = 0.5$ to be a good overall compromise.

Using multinomial sampling with replacement, we convert the re-scaled probabilities to a list of leaf indices. For each element in that list, we compute the a final sample position by randomly offsetting the center point of the selected leaf inside its volume. This improves quality, as appearance features (see Sec. 3.3) are regularized across a larger volume and not overwritten by hash-collisions.

For inference, we extend this scheme by sampling multiple point clouds, rasterizing them into 2D feature maps (see Sec. 3.4), and averaging the features for each pixel. This is similar to standard multisampling techniques for anti-aliasing in rendering.

Viewpoint-Independent Sampling. Motivated by the observation that sampling an implicit point cloud takes up more than half of the rendering time during inference, we want to pre-extract a global point cloud for all viewpoints. For

this, we use Eq. (4) but omit the factors $\mathbb{1}_{visible}$ and d_i . Again using multinomial sampling with replacement, we extract the number of samples for each leaf. To increase stability, we then use the 3D Halton sequence [22] for determining the final position of each sample. We consider this another advantage of our method: Our implicit formulation can be used to extract large point clouds without having to store them on disk.

3.3 Appearance Representation

After sampling, we retrieve $M + 1$ appearance features from a multi-resolution hash grid for each point. Before querying with each points position, we apply the spherical contraction by Barron *et al.* [4] to increase the relative capacity of our model near the center of the scene, *i.e.* the best-observed regions during optimization. Of the retrieved per-point features, the first one is converted to a valid opacity value $\alpha_h \in [0, 1]$ as per

$$\alpha_h = 1 - e^{-e^x}, \quad (5)$$

as we observe improved results when optimizing opacity as log-space density (also noted by Müller *et al.* [36]). The remaining M features are used as coefficients for SH evaluations to produce a view-dependent feature for each point. In practice, we use SH of degree 2 and 4D view-dependent output features, resulting in $M = 36$ SH coefficients per point. As our background model, we employ a small MLP that computes a 4D feature for each pixel using the corresponding SH-encoded viewing direction as input.

For our implementation, we use the exceptionally fast implementation by Müller *et al.* [36].

3.4 Differentiable Bilinear Point Splatting

Prior work on point rasterization has demonstrated that point rendering for radiance fields can be very fast and yield great results [17, 27, 43]. However, using one-pixel point rendering (projecting and discretizing points to one pixel) leads to aliasing as well as the need for approximate gradients [43]. To avoid this, we opt to use a bilinear formulation, that is we splat each point to its closest 2×2 neighbors after projection. Thus, for a sampled point $p_w = (x, y, z)^T$, we project it to the image coordinates $p = (u, v, d)^T$ with

$$p = P \cdot V \cdot p_w, \quad (6)$$

with P the intrinsic and V the extrinsic camera matrices. For the 2×2 closest pixel’s center points $p_{i \in \{0..3\}} = (u_i, v_i)^T$ we then compute the opacities with

$$\alpha = \alpha_h \cdot (1 - |u - u_i|) \cdot (1 - |v - v_i|). \quad (7)$$

This causes the points contribution to be weighted correctly based on their projected position. We then use this to blend (see Eq. (1)) all points \mathcal{N} in depth order and thus create three images of progressively lower resolution [1, 43].

This bilinear splatting approach has three advantages: (1) We obtain more robust gradients, (2) improve temporal stability of the rendering pipeline, and (3) the rasterized images contain less holes which eases the job of the hole-filling CNN. Concurrent work by Franke *et al.* [17] uses a similar splatting approach but instead interpolates trilinearly into an image pyramid based on a learned per-point radius. Our implicit point cloud enables us to render high-quality feature maps without the need for interpolation w.r.t. a third dimension.

3.5 Post-Processing

For decoding, we use a standard three-layer U-Net architecture with a single residual block based on *Fast Fourier Convolution (FFC)* [10]. We find that this change enhances reconstruction regarding high-frequency details. For challenging, *e.g.*, auto-exposed outdoor scenes, we append the differentiable tone mapping module proposed by Rückert *et al.* [43] to our pipeline.

3.6 Optimization Loss

Inspired by prior works [21,27], we combine a per-pixel loss and two established image-space loss functions:

$$\mathcal{L} = \mathcal{L}_R + \mathcal{L}_{D\text{-SSIM}} + \lambda_{vgg} \cdot \mathcal{L}_{VGG} + \lambda_{decay} \cdot \mathcal{L}_{Reg}. \quad (8)$$

Specifically, we use the robust loss \mathcal{L}_R [2] with $\alpha = 0$ and $c = 0.2$ as our per-pixel loss as well as D-SSIM and VGG [26] losses which are commonly attributed with a more closer resemblance of human perception. For regularization we follow Barron *et al.* [5] and impose a normalized weight decay on the parameters of the multi-resolution hash grid. We use $\lambda_{vgg} = 0.075$ and $\lambda_{decay} = 0.1$.

4 Experiments

We conduct multiple experiments to evaluate the proposed method of using an implicit point model for radiance field optimization and rendering.

4.1 Datasets and Baselines

For evaluation, we use a total of 17 real scenes featuring a broad spectrum of challenges regarding both geometric and photometric aspects. The Mip-NeRF360 dataset [4] contains five outdoor and four indoor scenes captured with fixed exposure and white balance settings. We further use all eight scenes from the *intermediate* set of the Tanks and Temples dataset [29]. It was captured without fixed camera settings and presents challenges regarding photometric variation that complicate reconstruction, providing relevant insights for in-the-wild performance. We use the established 7:1 train/test split [4] for all scenes. We optimize for 50,000 iterations and render an image for a single viewpoint in each of those.

Table 1: Quantitative comparisons on the Mip-NeRF360 [4] and Tanks and Temples [29] datasets. The three best results are highlighted in green in descending order of saturation. Alongside our default configuration that uses 33M samples (*Ours*) we also provide metrics for our method when trained with less samples (*16M* and *8M*). Furthermore, we report results using a pre-extracted point cloud for inference (*pre-ex.*).

Method	Mip-NeRF360			Tanks&Temples			Train hrs↓	Render fps↑	Size GB↓
	LPIPS↓	SSIM↑	PSNR↑	LPIPS↓	SSIM↑	PSNR↑			
Instant-NGP [36]	0.380	0.698	25.61	0.438	0.737	21.82	0.08	5.7	0.1
ADOP [43]	0.259	0.723	23.54	0.236	0.802	21.69	7.00	67.6	0.53
TRIPS [17]	0.213	0.778	25.94	0.229	0.831	22.62	4.00	90.0	0.76
3DGS [27]	0.254	0.814	27.20	0.276	0.866	25.27	0.50	194.2	0.58
Zip-NeRF [5]	0.219	0.828	28.56	0.233	0.878	26.75	5.00	0.2	0.9
Ours	0.167	0.842	28.09	0.187	0.878	25.29	10.8	2.1	1.1
Ours (16M)	0.179	0.836	27.83	0.210	0.866	24.80	7.47	3.7	1.1
Ours (8M)	0.197	0.825	27.67	0.256	0.845	24.26	5.75	5.8	1.1
Ours (pre-ex.)	0.262	0.737	21.66	0.377	0.747	15.46	5.75	20.1	1.1

We compare our method against Instant-NGP [36], ADOP [43], TRIPS [17], 3D Gaussian Splatting [27], and the current state-of-the-art in terms of image quality Zip-NeRF [5]. We use the images kindly provided by the authors of the respective publications when available – otherwise we use the official implementation to generate the images – and compute all image quality metrics under identical conditions. All methods use an RTX 4090 when memory was sufficient, otherwise an A100 was used.

4.2 Results

We show quantitative results for the scenes from Mip-NeRF360 and Tanks and Temples in Tab. 1 as well as qualitative comparisons in Fig. 3. In terms of image quality metrics, our method clearly outperforms previous point-based techniques (TRIPS and 3DGS) and achieves similar quality as Zip-NeRF on both datasets. Visually, we observe that our method outperforms all baselines w.r.t. representing fine details, which is also represented in its excellent score in the LPIPS metric. Good examples for such cases are the swing chains, the spokes of the bicycle, the grass within the flowers scene, and the text on the family statue. We also observe less artifacts in the Tanks and Temples renderings in comparison to 3DGS and Zip-NeRF and deduce that our approach is better suited for capturing view-dependent effects under varying photometric conditions. An example for this is the reflection on the base of the horse statue.

All our models use $4\times$ multisampling for inference, which results in up to 528 million blended splats per image for our largest configuration that uses 33M samples in each training iteration. We want to highlight the results of our 8M configuration. It still provides excellent quality, while training in just over 5 hours and blending 128 million splats at interactive frame rates of 6 fps – all on a single RTX 4090 GPU. By applying our view-independent sampling algorithm to pre-extract a point cloud for inference, we can further boost rendering performance.

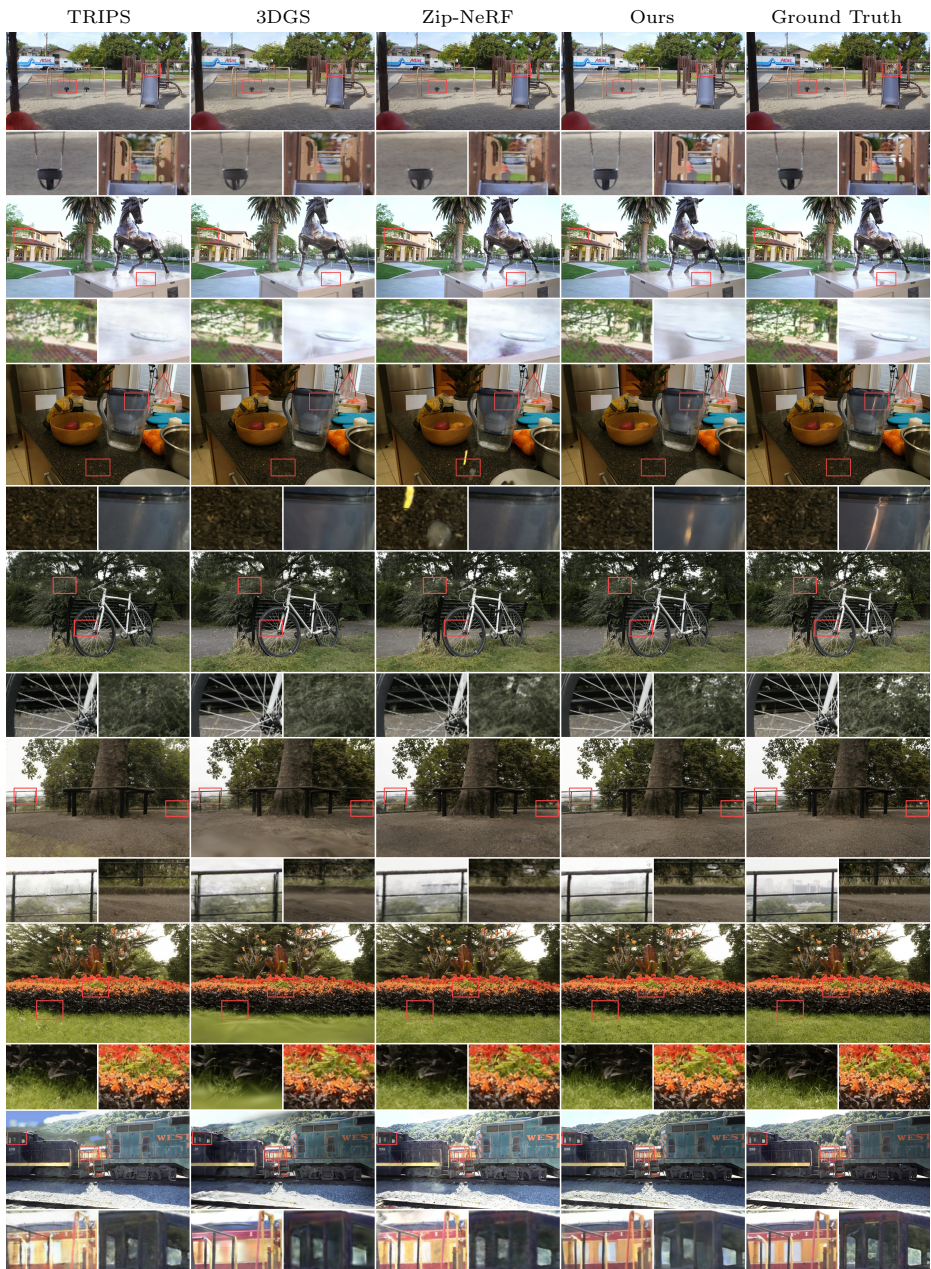

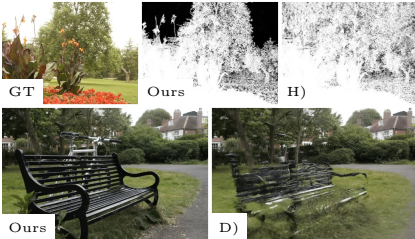


Fig. 3: Visual comparisons showing our method better represents fine details while having less failure cases in comparison to all baselines.

Configuration	LPIS↓	SSIM↑	PSNR↑
A) No D-SSIM Loss	0.210	0.720	24.87
B) No VGG Loss	0.249	0.747	24.97
C) No Weight Decay	0.211	0.733	24.88
D) No Subdivision	0.486	0.403	19.44
E) No Bilinear Splatting	0.312	0.591	22.48
F) No Multisampling	0.211	0.725	24.63
G) No SfM Prior	0.205	0.742	24.96
H) No Background Model	0.203	0.748	25.17
I) No FFC Block	0.208	0.745	25.06
Ours (8M)	0.201	0.749	25.11
+ Tone Mapper	0.199	0.753	25.09



(a) Quality metrics



(b) Visual comparisons

Fig. 4: Model ablations computed on the outdoor scenes from the Mip-NeRF360 dataset.

We further show approximates for the training time, inference frame rate, and resulting model size in Tab. 1. Our method requires slightly longer training than the recent Zip-NeRF and TRIPS. Like other NeRF-based methods such as Zip-NeRF, our model always has the same size (1.1 GB), whereas point-based methods such as 3DGS require up to 2 GB of storage depending on the scene. Regarding inference fps, our method is roughly an order of magnitude faster than Zip-NeRF but outperformed by explicit point-based approaches. We are confident, however, that an optimized implementation in CUDA can overcome some of the gap, as specialized rendering methods for explicit point clouds showed for similar amounts of points [46].

Ablations. Figure 4 shows ablations of our 8M model computed on the five outdoor scenes from the Mip-NeRF360 dataset. A) – C) dissect our loss function showing that each term has a meaningful contribution. For D), we omit octree subdivision during optimization, which greatly hinders reconstruction of fine details close to the camera while having no visible impact on far away objects. E) and F) validate the effectiveness of our bilinear splatting approach as well as the point cloud multisampling during inference. Next, G) shows that our method works well even without initial SfM points for sampling probability initialization. For H), we observe that leaving out the background model barely impacts metrics but results in sampling points in the sky (see alpha maps in Fig. 4) which results in “floaters” upon visual inspection. Lastly, I) indicates the residual FFC block in the U-Net enhances performance for high-frequency details, which is only partly captured by metrics. We also observe a minimal performance improvement using learned tone mapping, which we omit by default as the Mip-NeRF360 outdoor scenes do not exhibit the targeted photometric variations.

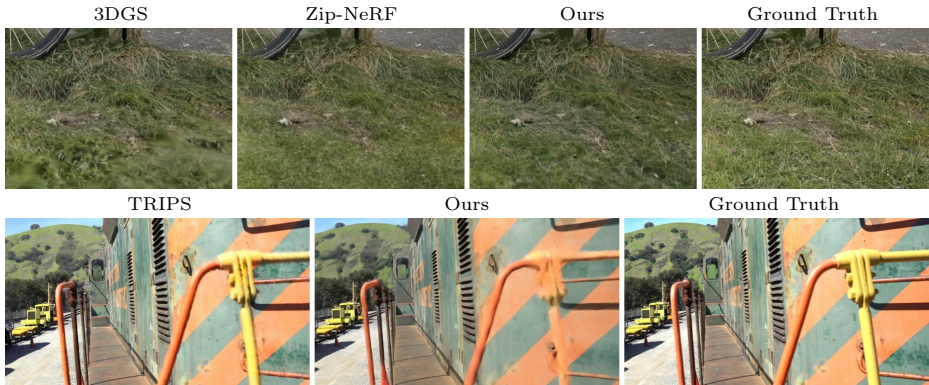


Fig. 5: Limitations. Reconstructions lack fine geometric detail near the camera (*top*) and our method performs slightly worse on datasets exhibiting high photometric variation (*bottom*).

5 Discussion

The experiments confirm that our approach works well on common benchmarks, outperforming previous state-of-the-art in terms of image quality, while also rendering at interactive frame rates. However, our method is not without limitations. We observe INPC is sometimes unable to reconstruct fine geometric detail close to the camera, a limitation shared with existing methods such as 3DGS and Zip-NeRF. Also, our method is less robust when reconstructing scenes with high amounts of photometric variation compared to the concurrent TRIPS, as its fixed point cloud reduces the degrees of freedom during optimization. For visualizations see the first and second row of Fig. 5 respectively. Similar to previous works that used a CNN for post-processing rasterizer outputs [16, 43], we identify temporal stability as a minor issue during inference (see our supplemental video). To overcome these limitations, we infer two main avenues for how INPC could be improved in the future from our results. As extracting a global point cloud greatly boost frame rates during inference, the optimization pipeline could be adjusted to facilitate viewpoint-independent sampling, *e.g.*, by encouraging binary opacity values as done by Reiser *et al.* [40]. We also think the underlying octree-based data structure could be improved. Lifting our implementation’s limitation of 256^3 active leaf nodes in the octree, in combination with improved routines for subdivision, updating, and pruning, is likely to further boost reconstruction quality.

6 Conclusion

In this work, we have introduced Implicit Neural Point Clouds, a concept fusing NeRF- and point-based radiance fields, utilizing the advantages of both. Our INPC retains favorable optimization properties of NeRF by representing a point

cloud inside an octree-based probability field for point positions and an implicit appearance model. The evaluation shows that our method improves upon the previous state-of-the-art method in terms of image quality, while also enabling rendering at interactive frame rates on consumer-grade hardware. We believe that the implicit point cloud representation as well as other ideas presented here can enable future work towards further closing the gap between best-quality and real-time radiance field approaches.

Acknowledgements. We would like to thank Peter Kramer for his help with the video as well as Timon Scholz for helping with the implementation of our viewer. The authors gratefully acknowledge financial support by the German Research Foundation (DFG) for funding of the projects “Immersive Digital Reality” (ID 283369270) and “Real-Action VR” (ID 523421583) as well as the scientific support and HPC resources provided by the Erlangen National High Performance Computing Center (NHR@FAU) of the Friedrich-Alexander-Universität Erlangen-Nürnberg (FAU) under the NHR project b162dc. NHR funding is provided by federal and Bavarian state authorities. NHR@FAU hardware is partially funded by the DFG (ID 440719683). Linus Franke was supported by the Bayerische Forschungsförderung (Bavarian Research Foundation) AZ-1422-20.

References

1. Aliev, K.A., Sevastopolsky, A., Kolos, M., Ulyanov, D., Lempitsky, V.: Neural point-based graphics. In: ECCV (2020). https://doi.org/10.1007/978-3-030-58542-6_42
2. Barron, J.T.: A general and adaptive robust loss function. In: Proceedings of the IEEE/CVF Conference on Computer Vision and Pattern Recognition. pp. 4331–4339 (2019)
3. Barron, J.T., Mildenhall, B., Tancik, M., Hedman, P., Martin-Brualla, R., Srinivasan, P.P.: Mip-nerf: A multiscale representation for anti-aliasing neural radiance fields. ICCV (2021). <https://doi.org/10.1109/ICCV48922.2021.00580>
4. Barron, J.T., Mildenhall, B., Verbin, D., Srinivasan, P.P., Hedman, P.: Mip-nerf 360: Unbounded anti-aliased neural radiance fields. CVPR (2022). <https://doi.org/10.1109/CVPR52688.2022.00539>
5. Barron, J.T., Mildenhall, B., Verbin, D., Srinivasan, P.P., Hedman, P.: Zip-nerf: Anti-aliased grid-based neural radiance fields. In: ICCV. pp. 19640–19648 (October 2023). <https://doi.org/10.1109/ICCV51070.2023.01804>
6. Chaurasia, G., Duchene, S., Sorkine-Hornung, O., Drettakis, G.: Depth synthesis and local warps for plausible image-based navigation. ACM Transactions on Graphics (TOG) **32**(3), 1–12 (2013)
7. Chen, A., Xu, Z., Geiger, A., Yu, J., Su, H.: TensorRF: Tensorial radiance fields. In: ECCV (2022). https://doi.org/10.1007/978-3-031-19824-3_20
8. Chen, A., Xu, Z., Zhao, F., Zhang, X., Xiang, F., Yu, J., Su, H.: Mvsnerf: Fast generalizable radiance field reconstruction from multi-view stereo. In: Proceedings of the IEEE/CVF International Conference on Computer Vision. pp. 14124–14133 (2021)

9. Chen, Z., Funkhouser, T., Hedman, P., Tagliasacchi, A.: Mobilenerf: Exploiting the polygon rasterization pipeline for efficient neural field rendering on mobile architectures. In: Proceedings of the IEEE/CVF Conference on Computer Vision and Pattern Recognition. pp. 16569–16578 (2023)
10. Chi, L., Jiang, B., Mu, Y.: Fast fourier convolution. *Advances in Neural Information Processing Systems* **33**, 4479–4488 (2020)
11. Chibane, J., Bansal, A., Lazova, V., Pons-Moll, G.: Stereo radiance fields (srf): Learning view synthesis for sparse views of novel scenes. In: Proceedings of the IEEE/CVF Conference on Computer Vision and Pattern Recognition. pp. 7911–7920 (2021)
12. Debevec, P., Yu, Y., Boshokov, G.: Efficient view-dependent ibr with projective texture-mapping. In: EG Rendering Workshop. vol. 4 (1998)
13. Ding, Y., Yuan, W., Zhu, Q., Zhang, H., Liu, X., Wang, Y., Liu, X.: Transmvsnet: Global context-aware multi-view stereo network with transformers. In: Proceedings of the IEEE/CVF Conference on Computer Vision and Pattern Recognition. pp. 8585–8594 (2022)
14. Duckworth, D., Hedman, P., Reiser, C., Zhizhin, P., Thibert, J.F., Lučić, M., Szeliski, R., Barron, J.T.: Smerf: Streamable memory efficient radiance fields for real-time large-scene exploration. arXiv preprint arXiv:2312.07541 (2023)
15. Eisemann, M., De Decker, B., Magnor, M., Bekaert, P., De Aguiar, E., Ahmed, N., Theobalt, C., Sellent, A.: Floating textures. In: *Computer graphics forum*. vol. 27, pp. 409–418. Wiley Online Library (2008)
16. Franke, L., Rückert, D., Fink, L., Innmann, M., Stamminger, M.: Vet: Visual error tomography for point cloud completion and high-quality neural rendering. In: SIGGRAPH Asia Conference Papers. Association for Computing Machinery, New York, NY, USA (December 2023)
17. Franke, L., Rückert, D., Fink, L., Stamminger, M.: Trips: Trilinear point splatting for real-time radiance field rendering. arXiv preprint arXiv:2401.06003 (2024)
18. Fridovich-Keil, S., Yu, A., Tancik, M., Chen, Q., Recht, B., Kanazawa, A.: Plenoxels: Radiance fields without neural networks. In: 2022 IEEE/CVF Conference on Computer Vision and Pattern Recognition (CVPR). pp. 5491–5500 (2022). <https://doi.org/10.1109/CVPR52688.2022.00542>
19. Fridovich-Keil, S., Yu, A., Tancik, M., Chen, Q., Recht, B., Kanazawa, A.: Plenoxels: Radiance fields without neural networks. In: CVPR (2022). <https://doi.org/10.1109/CVPR52688.2022.00542>
20. Gortler, S.J., Grzeszczuk, R., Szeliski, R., Cohen, M.F.: The Lumigraph. In: CGIT (1996). <https://doi.org/10.1145/237170.237200>
21. Hahlbohm, F., Kappel, M., Tauscher, J.P., Eisemann, M., Magnor, M.: Plenoptic-points: Rasterizing neural feature points for high-quality novel view synthesis. In: Grosch, T., Guthe, M. (eds.) *Proc. Vision, Modeling and Visualization (VMV)*. pp. 53–61. Eurographics (September 2023). <https://doi.org/10.2312/vmv.20231226>
22. Halton, J.H.: Algorithm 247: Radical-inverse quasi-random point sequence. *Commun. ACM* **7**(12), 701–702 (December 1964). <https://doi.org/10.1145/355588.365104>
23. Harrer, M., Franke, L., Fink, L., Stamminger, M., Weyrich, T.: Inovis: Instant novel-view synthesis. In: SIGGRAPH Asia Conference Papers. Association for Computing Machinery, New York, NY, USA (December 2023). <https://doi.org/10.1145/3610548.3618216>, <https://doi.org/10.1145/3610548.3618216>
24. Hedman, P., Philip, J., Price, T., Frahm, J.M., Drettakis, G., Brostow, G.: Deep blending for free-viewpoint image-based rendering. *ACM Transactions on Graphics (ToG)* **37**(6), 1–15 (2018)

25. Hornung, A., Kobbelt, L.: Interactive pixel-accurate free viewpoint rendering from images with silhouette aware sampling. In: Computer Graphics Forum. vol. 28, pp. 2090–2103. Wiley Online Library (2009)
26. Johnson, J., Alahi, A., Fei-Fei, L.: Perceptual losses for real-time style transfer and super-resolution. In: ECCV (2016). https://doi.org/10.1007/978-3-319-46475-6_43
27. Kerbl, B., Kopanas, G., Leimkühler, T., Drettakis, G.: 3D Gaussian splatting for real-time radiance field rendering. ACM TOG **42**(4) (July 2023). <https://doi.org/10.1145/3592433>
28. Kingma, D.P., Ba, J.: Adam: A method for stochastic optimization. In: ICLR (2015). <https://doi.org/10.48550/arXiv.1412.6980>
29. Knapitsch, A., Park, J., Zhou, Q.Y., Koltun, V.: Tanks and temples: Benchmarking large-scale scene reconstruction. ACM Transactions on Graphics **36**(4) (2017)
30. Kopanas, G., Drettakis, G.: Improving NeRF Quality by Progressive Camera Placement for Free-Viewpoint Navigation. In: Guthe, M., Grosch, T. (eds.) Vision, Modeling, and Visualization. The Eurographics Association (2023). <https://doi.org/10.2312/vmv.20231222>
31. Kopanas, G., Leimkühler, T., Rainer, G., Jambon, C., Drettakis, G.: Neural point catacaustics for novel-view synthesis of reflections. ACM TOG (2022). <https://doi.org/10.1145/3550454.3555497>
32. Kopanas, G., Philip, J., Leimkühler, T., Drettakis, G.: Point-based neural rendering with per-view optimization. CGF (2021). <https://doi.org/10.1111/cgf.14339>
33. Lassner, C., Zollhofer, M.: Pulsar: Efficient sphere-based neural rendering. In: CVPR (2021). <https://doi.org/10.1109/CVPR46437.2021.00149>
34. Mildenhall, B., Srinivasan, P.P., Tanck, M., Barron, J.T., Ramamoorthi, R., Ng, R.: NeRF: Representing scenes as neural radiance fields for view synthesis. In: ECCV (2020). <https://doi.org/10.1145/3503250>
35. Müller, T.: tiny-cuda-nn (April 2021), <https://github.com/NVlabs/tiny-cuda-nn>
36. Müller, T., Evans, A., Schied, C., Keller, A.: Instant neural graphics primitives with a multiresolution hash encoding. ACM TOG **41**(4) (July 2022). <https://doi.org/10.1145/3528223.3530127>
37. Neff, T., Stadlbauer, P., Parger, M., Kurz, A., Mueller, J.H., Chaitanya, C.R.A., Kaplanyan, A.S., Steinberger, M.: DOnERF: Towards Real-Time Rendering of Compact Neural Radiance Fields using Depth Oracle Networks. CGF (2021). <https://doi.org/10.1111/cgf.14340>
38. Penner, E., Zhang, L.: Soft 3D reconstruction for view synthesis. ACM Transactions on Graphics (TOG) **36**(6) (November 2017). <https://doi.org/10.1145/3130800.3130855>
39. Rakhimov, R., Ardelean, A.T., Lempitsky, V., Burnaev, E.: NPBG++: Accelerating neural point-based graphics. In: CVPR (2022). <https://doi.org/10.1109/CVPR52688.2022.01550>
40. Reiser, C., Garbin, S., Srinivasan, P.P., Verbin, D., Szeliski, R., Mildenhall, B., Barron, J.T., Hedman, P., Geiger, A.: Binary opacity grids: Capturing fine geometric detail for mesh-based view synthesis. arXiv preprint arXiv:2402.12377 (2024)
41. Reiser, C., Szeliski, R., Verbin, D., Srinivasan, P.P., Mildenhall, B., Geiger, A., Barron, J.T., Hedman, P.: Merf: Memory-efficient radiance fields for real-time view synthesis in unbounded scenes. SIGGRAPH (2023). <https://doi.org/10.1145/3592426>
42. Ronneberger, O., Fischer, P., Brox, T.: U-net: Convolutional networks for biomedical image segmentation. In: MICCAI (2015). https://doi.org/10.1007/978-3-319-24574-4_28

43. Rückert, D., Franke, L., Stamminger, M.: Adop: Approximate differentiable one-pixel point rendering. *ACM TOG* (2022). <https://doi.org/10.1145/3528223.3530122>
44. Rückert, D., Wang, Y., Li, R., Idoughi, R., Heidrich, W.: Neat: Neural adaptive tomography. *ACM Trans. Graph.* **41**(4) (July 2022). <https://doi.org/10.1145/3528223.3530121>, <https://doi.org/10.1145/3528223.3530121>
45. Schönberger, J.L., Frahm, J.M.: Structure-from-motion revisited. In: *CVPR*. pp. 4104–4113 (2016). <https://doi.org/10.1109/CVPR.2016.445>
46. Schütz, M., Kerbl, B., Wimmer, M.: Software rasterization of 2 billion points in real time. *Proceedings of the ACM on Computer Graphics and Interactive Techniques* **5**(3), 1–17 (2022)
47. Schütz, M., Kerbl, B., Wimmer, M.: Rendering point clouds with compute shaders and vertex order optimization. *Computer Graphics Forum* **40**(4), 115–126 (July 2021). <https://doi.org/10.1111/cgf.14345>
48. Schütz, M., Kerbl, B., Wimmer, M.: Software rasterization of 2 billion points in real time. *Proceedings of the ACM on Computer Graphics and Interactive Techniques* **5**(3), 1–17 (July 2022). <https://doi.org/10.1145/3543863>
49. Seitz, S.M., Curless, B., Diebel, J., Scharstein, D., Szeliski, R.: A comparison and evaluation of multi-view stereo reconstruction algorithms. In: *2006 IEEE computer society conference on computer vision and pattern recognition (CVPR'06)*. vol. 1, pp. 519–528. *IEEE* (2006)
50. Shum, H., Kang, S.B.: Review of image-based rendering techniques. In: *Visual Communications and Image Processing 2000*. vol. 4067, pp. 2–13. *SPIE* (2000)
51. Tancik, M., Mildenhall, B., Wang, T., Schmidt, D., Srinivasan, P.P., Barron, J.T., Ng, R.: Learned initializations for optimizing coordinate-based neural representations. In: *Proceedings of the IEEE/CVF Conference on Computer Vision and Pattern Recognition*. pp. 2846–2855 (2021)
52. Tewari, A., Thies, J., Mildenhall, B., Srinivasan, P., Tretschk, E., Yifan, W., Lassner, C., Sitzmann, V., Martin-Brualla, R., Lombardi, S., Simon, T., Theobalt, C., Nießner, M., Barron, J.T., Wetzstein, G., Zollhöfer, M., Golyanik, V.: *Advances in Neural Rendering*. *EG STAR* (2022). <https://doi.org/10.1111/cgf.14507>
53. Thies, J., Zollhöfer, M., Nießner, M.: Deferred neural rendering: Image synthesis using neural textures. *ACM TOG* (2019)
54. Turki, H., Ramanan, D., Satyanarayanan, M.: Mega-nerf: Scalable construction of large-scale nerfs for virtual fly-throughs. In: *Proceedings of the IEEE/CVF Conference on Computer Vision and Pattern Recognition*. pp. 12922–12931 (2022)
55. Vats, V.K., Joshi, S., Crandall, D.J., Reza, M.A., Jung, S.h.: Gc-mvsnet: Multi-view, multi-scale, geometrically-consistent multi-view stereo. In: *Proceedings of the IEEE/CVF Winter Conference on Applications of Computer Vision*. pp. 3242–3252 (2024)
56. Wang, X., Zhu, Z., Huang, G., Qin, F., Ye, Y., He, Y., Chi, X., Wang, X.: Mvster: Epipolar transformer for efficient multi-view stereo. In: *European Conference on Computer Vision*. pp. 573–591. *Springer* (2022)
57. Wei, Y., Liu, S., Rao, Y., Zhao, W., Lu, J., Zhou, J.: Nerfingmvs: Guided optimization of neural radiance fields for indoor multi-view stereo. In: *Proceedings of the IEEE/CVF International Conference on Computer Vision*. pp. 5610–5619 (2021)
58. Wiles, O., Gkioxari, G., Szeliski, R., Johnson, J.: Synsin: End-to-end view synthesis from a single image. In: *CVPR* (2020). <https://doi.org/10.1109/CVPR42600.2020.00749>
59. Xu, K., Sun, W.L., Dong, Z., Zhao, D.Y., Wu, R.D., Hu, S.M.: Anisotropic spherical gaussians. *ACM Transactions on Graphics (TOG)* **32**(6), 1–11 (2013)

60. Xu, Q., Xu, Z., Philip, J., Bi, S., Shu, Z., Sunkavalli, K., Neumann, U.: Point-nerf: Point-based neural radiance fields. In: CVPR (2022). <https://doi.org/10.1109/CVPR52688.2022.00536>
61. Yao, Y., Luo, Z., Li, S., Fang, T., Quan, L.: Mvsnet: Depth inference for unstructured multi-view stereo. In: Proceedings of the European conference on computer vision (ECCV). pp. 767–783 (2018)
62. Yariv, L., Hedman, P., Reiser, C., Verbin, D., Srinivasan, P.P., Szeliski, R., Barron, J.T., Mildenhall, B.: Baked sdf: Meshing neural sdfs for real-time view synthesis. arXiv (2023)
63. Yifan, W., Serena, F., Wu, S., Öztireli, C., Sorkine-Hornung, O.: Differentiable surface splatting for point-based geometry processing. ACM Transactions on Graphics (TOG) **38**(6), 1–14 (2019)
64. Yu, A., Li, R., Tancik, M., Li, H., Ng, R., Kanazawa, A.: PlenOctrees for real-time rendering of neural radiance fields. In: ICCV (2021). <https://doi.org/10.1109/ICCV48922.2021.00570>
65. Yu, A., Ye, V., Tancik, M., Kanazawa, A.: pixelNeRF: Neural radiance fields from one or few images. In: Proceedings of the IEEE/CVF Conference on Computer Vision and Pattern Recognition. pp. 4578–4587 (2021). <https://doi.org/10.1109/CVPR46437.2021.00455>
66. Zhou, Y., Barnes, C., Lu, J., Yang, J., Li, H.: On the continuity of rotation representations in neural networks. In: Proceedings of the IEEE/CVF conference on computer vision and pattern recognition. pp. 5745–5753 (2019)
67. Zuo, Y., Deng, J.: View synthesis with sculpted neural points. In: The Eleventh International Conference on Learning Representations (2022)

A Implementation

We believe that the flexibility of our implicit point cloud could prove to be useful for future work. Here, we try to support such work by providing all details of our implementation.

A.1 Overview

We implement our method using PyTorch with the only exception being our differentiable rasterization module for which we implement a re-usable PyTorch extension in C++/CUDA. Furthermore, we use multiple libraries that provide efficient implementations for parts of our pipeline. For the multi-resolution hash grid as well as the background MLP, we use the implementation provided with the *tiny-cuda-nn* (TCNN) framework [35]. As our optimizer, we use the fused ADAM [28] implementation provided by the NVIDIA Apex library. To reduce computation time of the CNN, we also make use of PyTorch’s automatic mixed precision package and scale FP16 gradients by a fixed factor of 128 during the backward pass.

A.2 Optimization Details

For ADAM, we use $\beta_1 = 0.9$, $\beta_2 = 0.99$, $\epsilon = 1e-15$, and disable weight decay. The learning rates for all parameters are exponentially decayed during the optimization.

For the hash grid and MLP parameters, we decay the learning rate from 1e-2 to 3e-4, while CNN parameter learning rates are decayed from 3e-4 to 5e-5.

When using differentiable tone mapping as proposed by Rückert *et al.* [43], we follow the authors and only activate the sub-modules for exposure and camera response. Similar to Rückert *et al.* [43], these parameters are updated with a fixed learning rate of 5e-4 and 1e-3 respectively. However, we use a warm-up strategy [3] where the learning rate is multiplied with a factor that is cosine-decayed from 0.01 to 1 during the first 5,000 iterations. This is slightly different from the original version that simply disabled tone mapping optimization during the first few iterations.

A.3 Dataset Details

For all scenes, we apply a world-space transformation [4] to all camera poses so that they fit inside a cube $[-1, 1]^3$. We apply the same transformation to the SfM point cloud if it is used. For the near and far planes we use 0.01 and 100 respectively. For each scene, we define $b_{\min}, b_{\max} \in \mathbb{R}^3$ as the axis-aligned bounding box of the SfM point cloud and enlarge the result by 10% for increased robustness.

A.4 Point Probability Octree Details

Initialization. Given a desired initial resolution R and an axis-aligned bounding box $b_{\min}, b_{\max} \in \mathbb{R}^3$ of the scene, we initialize our octree-based data structure as a regular grid of cube-shaped voxels. These 3D voxels are the initial leaf nodes of \mathcal{P} . For each leaf node, we store its center $c_i \in \mathbb{R}^3$ in world space, current subdivision level $l_i \in \mathbb{N}_0$, and probability $p_i \in [0, 1]$. We limit values of R to powers of 2 and can thus initialize the initial subdivision level as $\log_2(N)$ for all leaf nodes.

Depth Calculation. For our view-specific re-weighting scheme, we need to obtain a view-specific depth value $d_i \in [0, 1]$ for each leaf node. To this end, we compute the distance from the image plane to a leaf center via:

$$d_i = \max\left(\frac{|z_{view} - \text{near}|}{\text{far} - \text{near}}, \tau_d\right). \quad (9)$$

In practice, we use 10^{-8} for τ_d to prevent extreme cases of oversampling close to the camera.

A major difficulty comes from dealing with those leaves whose volume intersects the faces of the viewing frustum. For these, it is possible that positions generated by our sampling scheme lie outside the frustum. To this end, we simply re-sample until the desired number of samples is reached. During inference, we use multisampled point clouds and can therefore omit resampling, which also boosts performance.

Listing 1 Hash grid configuration for the *tiny-cuda-nn* implementation [35].

```

encoding_config = {
  'otype': 'Grid',
  'type': 'Hash',
  'n_levels': 10,
  'n_features_per_level': 4,
  'log2_hashmap_size': 23,
  'base_resolution': 16,
  'per_level_scale': 2.0,
  'interpolation': 'Linear',
}
network_config = {
  'otype': 'FullyFusedMLP',
  'activation': 'ReLU',
  'output_activation': 'None',
  'n_neurons': 64,
  'n_hidden_layers': 1,
}

```

A.5 TCNN Details

For our multi-resolution hash grid, we tested the configurations used by Instant-NGP [36], BakedSDF [62], and Zip-NeRF [5]. Our resulting configuration is shown in Listing 1. It is similar to the one used by Zip-NeRF [5], but we increase the hashmap size from 21 to 23 (see Appendix B for ablations). For the background MLP we also use the fully-fused implementation of the TCNN framework [35]. It has four hidden layers with 128 neurons each and uses ReLU activations. For each pixel, we encode its normalized viewing direction using spherical harmonics of degree three before inputting into the MLP. Note that in TCNN this means using 'degree': 4 and converting input directions to $[0, 1]^3$.

A.6 Bilinear Splatting Details

Prior work on point rasterization has demonstrated that software implementations are a) very fast [47, 48] compared to hardware implementations, *e.g.*, GL_POINTS, and b) allow for backward pass implementations suited for gradient-based optimization [33, 43]. Motivated by these insights, we set out to design our own rasterization module in an effort to adapt it to the needs of our remaining pipeline.

Part of why MLP-based radiance fields works so well is the fully differentiable color accumulation of multiple samples for a given pixel. While NeRF uses a volume rendering-based formulation, recent successful point-based methods [17, 27] use conventional α -blending, which is similarly favorable for gradient-based optimization. We deem the extra cost of sorting points worthy w.r.t. to the superior optimization properties.

The second consideration is the selection of points blended into each pixel. Typically, each point is projected onto a single pixel using the extrinsic and intrinsic camera matrices. Using this approach, the unstructured and disconnected nature of point clouds may cause large holes in the resulting image. To this end, we follow the common practice of optimizing a hole-filling CNN alongside the rest of our model, which helps a great deal but causes other downstream problems

such as temporal instabilities. However, other approaches for addressing the issue exist. Among these, splatting is a well-established technique in rasterization-based rendering where the same point may influence multiple pixels at once. Furthermore, splatting ameliorates the problems arising from the need of discrete pixel coordinates for drawing each point. While, mathematically speaking, a point is always projected onto a single pixel, giving the same weight to points projected near pixel boundaries and those projected into the center of a pixel can be problematic for gradient-based optimization. We therefore splat each point into the four closest pixel and achieve this by downweighting its opacity using bilinear interpolation before blending it into each pixel (*cf.* main paper). The full algorithm, which we implement in CUDA to achieve accelerated rendering times, can be written as shown in Algorithm 1. We use the NVIDIA CUB library

Algorithm 1 GPU rasterization with bilinear point splatting and α -blending

C : camera model

P, A, F : point positions, opacities, and features

function RASTERIZE(C, P, A, F)

$P' \leftarrow \text{ProjectAndCull}(P, C)$

$A', K, N \leftarrow \text{BilinearSplatting}(P', A)$

▷ Splat Opacities, Keys, and Counts

$L \leftarrow \text{ExclusiveSum}(N)$

▷ Splat Indices

$\text{RadixSortPairs}(K, L)$

▷ Global Sort

$I \leftarrow \text{BlendSortedSplats}(A', F, L, N)$

▷ Per-Pixel α -Blending

return I

end function

for the exclusive sum as well as the global radix sorting of key/value pairs. As we identify global memory accesses to be the main performance bottleneck for our blending kernel, we implement it using CUDA’s warp-level primitives distributing the workload for each pixel over a full warp of 32 threads. The blending weight computation required for updating \mathcal{P} as well as the spherical harmonics computations are fused into this pipeline. During optimization, we store the bilinear interpolation weights, per-pixel point counts, and sorted key/index buffers for the backward pass. To compute per-splat gradients we process them in the same order as in the forward pass. We obtain a per-point gradient by combining its four splat gradients in a weighted sum according to the respective bilinear interpolation weights.

During the optimization, we use multiple resolutions of features maps as input for our rendering CNN. We keep the implementation simple and simply create multiple instances of our rasterization module for each resolution level.

A.7 CNN Details

For the rendering network, we use a standard three-layer U-Net architecture with 64 initial filters, GELU activations, average pooling for downsampling, and bilinear

interpolation followed by a point-wise convolution – and zero-padding if needed – for upsampling. In the contracting path, we concatenate multi-resolution feature maps produced by our rasterizer to the output of the average pooling operation. One important change is the introduction of a single residual block based on *Fast Fourier Convolution (FFC)* [10]. We use the authors’ implementation with $\alpha_{in}, \alpha_{out} = 0.75$ and no further modifications.

B Additional Ablations

In Tab. 2, we show additional model ablations computed by running our 8M configuration on the five outdoor scenes from the Mip-NeRF360 dataset [4]. In addition to including optimization time, inference frame rate, and model size for the ablations from the main paper, we also ablate other components of our pipeline in detail. We show the impact of omitting parts of our view-specific re-weighting scheme, using different hash map sizes for \mathcal{A} , and results without the spherical contraction proposed by Barron *et al.* [4].

We also analyze different representations for capturing view-dependent effects. Not modeling view-dependence at all produces the worst results and using one spherical harmonics (SH) degree less impacts quality only on a few scenes. We also show the impact of not fusing the SH computations into the rasterization module. Alternatives to SH such as spherical Gaussians (SG) [62, 64] and anisotropic spherical Gaussians (ASG) [59] perform worse in our tests. For SG, we encode the lobe width inside the length of the mean vector, which results in 25 and 32 parameters per point with three and four lobes respectively. For ASG, we use a 6D feature vector representing a rotation matrix [66] for each lobe and use the basis vectors of this matrix to model the anisotropic extent. This results in 15 parameters per point for a configuration with a single ASG lobe.

Lastly, we analyze the impact of different U-Net configurations. Using less initial filters as well as using more or less layers performs worse. Replacing the standard convolution blocks with *gated convolutions* as done by Rückert *et al.* [43] provides no benefits for our method. Using no multi-resolution inputs for the U-Net slightly reduces image quality but accelerates rendering.

C Per-Scene Results

In Tab. 3, we show per-scene image quality metrics for the Mip-NeRF360 dataset [4]. In Tab. 4, we do the same for the *intermediate* set of the Tanks and Temples dataset [29]. For Mip-NeRF360 [4], we follow the common practice of using $4\times$ downsampling for the five outdoor scenes and $2\times$ downsampling for the four indoor scenes. For the eight scenes from Tanks and Temples [29] no downsampling was used.

Table 2: Model ablations computed on the five Mip-NeRF360 outdoor scenes.

Configuration	LPIPS↓	SSIM↑	PSNR↑	Train (hrs)↓	Render (fps)↑	Size (GB)↓
A) No D-SSIM Loss	0.210	0.720	24.87	5.6	5.8	1.1
B) No VGG Loss	0.249	0.747	24.97	4.9	5.8	1.1
C) No Weight Decay	0.211	0.733	24.88	5.0	5.8	1.1
D) No Subdivision	0.486	0.403	19.44	4.75	5.9	0.87
E) No Bilinear Splatting	0.312	0.591	22.48	5.4	10.2	1.1
F) No Multisampling	0.211	0.725	24.63	5.75	17.8	1.1
G) No SfM Prior	0.205	0.742	24.96	5.75	5.8	1.1
H) No Background Model	0.203	0.748	25.17	5.5	5.9	1.1
I) No FFC Block	0.208	0.745	25.06	5.6	5.9	1.1
\mathcal{P} : No Viewpoint Bias	0.518	0.437	19.10	3.1	5.9	0.98
\mathcal{P} : No Depth Re-weighting	0.235	0.704	24.37	5.7	5.8	1.1
\mathcal{P} : No Size Re-weighting	0.206	0.737	24.80	5.7	5.8	1.1
\mathcal{A} : Hashmap Size 2^{21}	0.214	0.735	24.81	4.9	6.1	0.52
\mathcal{A} : Hashmap Size 2^{22}	0.207	0.742	24.92	5.2	6.0	0.73
\mathcal{A} : No Space Contraction	0.252	0.689	24.25	5.9	6.0	1.1
\mathcal{A} : No View-Dependence	0.211	0.732	24.36	5.4	6.0	1.1
\mathcal{A} : SH Degree 1	0.200	0.751	25.10	5.5	4.6	1.1
\mathcal{A} : SH PyTorch	0.201	0.746	25.01	5.8	4.5	1.1
\mathcal{A} : 3 SG Lobes	0.202	0.746	24.88	5.9	4.6	1.1
\mathcal{A} : 4 SG Lobes	0.204	0.744	24.85	6.1	4.3	1.1
\mathcal{A} : 1 ASG Lobe	0.207	0.739	24.62	6.0	4.7	1.1
U-Net: 32 Initial Filters	0.215	0.735	24.63	5.2	6.1	1.1
U-Net: 2 Layers	0.218	0.731	24.58	5.4	6.5	1.1
U-Net: 4 Layers	0.206	0.743	24.96	6.1	4.1	1.2
U-Net: No Multi-Res. Input	0.213	0.742	24.89	5.2	9.0	1.1
U-Net: Gated Convolutions	0.209	0.744	24.91	5.8	5.2	1.1
Ours (4M)	0.238	0.712	24.26	4.7	10.3	1.1
Ours (8M)	0.201	0.749	25.11	5.75	5.8	1.1
+ Tone Mapper	0.199	0.753	25.09	5.8	5.8	1.1

Table 3: Per-scene image quality metrics for the Mip-NeRF360 dataset [4] separated into outdoor and indoor scenes. The three best results are highlighted in green in descending order of saturation.

LPIPS↓ on Mip-NeRF360 [4]									
Method	<i>Bicycle</i>	<i>Flowers</i>	<i>Garden</i>	<i>Stump</i>	<i>Treehill</i>	<i>Bonsai</i>	<i>Counter</i>	<i>Kitchen</i>	<i>Room</i>
Instant-NGP [36]	0.478	0.466	0.289	0.474	0.496	0.258	0.368	0.249	0.340
ADOP [43]	0.250	0.361	0.203	0.305	0.354	0.223	0.264	0.221	0.241
TRIPS [17]	0.223	0.318	0.183	0.309	0.308	0.153	0.206	0.154	0.197
3DGS [27]	0.229	0.366	0.118	0.244	0.367	0.253	0.262	0.158	0.289
Zip-NeRF [5]	0.228	0.309	0.127	0.236	0.281	0.196	0.223	0.134	0.238
Ours	0.160	0.215	0.087	0.181	0.224	0.139	0.183	0.125	0.190
Ours (16M)	0.177	0.224	0.094	0.196	0.235	0.155	0.197	0.133	0.196
Ours (8M)	0.188	0.245	0.100	0.227	0.244	0.180	0.237	0.139	0.214
Ours (pre-ex.)	0.257	0.277	0.124	0.354	0.322	0.237	0.307	0.185	0.292
SSIM↑ on Mip-NeRF360 [4]									
Method	<i>Bicycle</i>	<i>Flowers</i>	<i>Garden</i>	<i>Stump</i>	<i>Treehill</i>	<i>Bonsai</i>	<i>Counter</i>	<i>Kitchen</i>	<i>Room</i>
Instant-NGP [36]	0.513	0.485	0.706	0.591	0.544	0.904	0.816	0.856	0.870
ADOP [43]	0.665	0.494	0.741	0.666	0.556	0.818	0.769	0.737	0.839
TRIPS [17]	0.704	0.502	0.773	0.681	0.591	0.899	0.845	0.850	0.883
3DGS [27]	0.770	0.602	0.869	0.774	0.637	0.938	0.905	0.921	0.913
Zip-NeRF [5]	0.772	0.637	0.863	0.788	0.674	0.952	0.905	0.929	0.929
Ours	0.804	0.660	0.888	0.816	0.679	0.950	0.914	0.931	0.933
Ours (16M)	0.789	0.662	0.878	0.801	0.679	0.949	0.912	0.928	0.930
Ours (8M)	0.781	0.647	0.874	0.765	0.676	0.941	0.888	0.923	0.929
Ours (pre-ex.)	0.689	0.570	0.827	0.603	0.578	0.848	0.831	0.847	0.840
PSNR↑ on Mip-NeRF360 [4]									
Method	<i>Bicycle</i>	<i>Flowers</i>	<i>Garden</i>	<i>Stump</i>	<i>Treehill</i>	<i>Bonsai</i>	<i>Counter</i>	<i>Kitchen</i>	<i>Room</i>
Instant-NGP [36]	22.21	20.68	25.14	23.47	22.42	30.69	26.69	29.48	29.71
ADOP [43]	22.60	19.68	24.85	24.18	20.99	24.33	23.09	23.61	25.97
TRIPS [17]	23.47	19.44	25.38	24.17	22.04	28.71	27.00	27.66	29.07
3DGS [27]	25.25	21.52	27.41	26.55	22.49	31.98	28.69	30.32	30.63
Zip-NeRF [5]	25.85	22.33	28.22	27.35	23.95	34.79	29.12	32.36	33.04
Ours	25.81	22.16	28.34	27.56	23.14	32.52	29.21	31.16	32.93
Ours (16M)	25.17	22.28	27.89	26.96	23.20	32.52	29.17	30.76	32.55
Ours (8M)	25.40	22.07	28.05	26.49	23.56	31.57	28.63	30.55	32.68
Ours (pre-ex.)	23.09	20.74	25.62	22.81	21.91	22.09	20.32	16.73	21.64

Table 4: Per-scene image quality metrics for the Tanks and Temples dataset [29]. The three best results are highlighted in green in descending order of saturation.

LPIPS↓ on Tanks and Temples [29]								
Method	Family	Francis	Horse	Lighthouse	M60	Panther	Playground	Train
Instant-NGP [36]	0.413	0.439	0.458	0.439	0.367	0.355	0.547	0.487
ADOP [43]	0.203	0.233	0.201	0.242	0.225	0.219	0.231	0.302
TRIPS [17]	0.176	0.266	0.182	0.277	0.204	0.191	0.222	0.267
3DGS [27]	0.236	0.344	0.239	0.291	0.244	0.241	0.291	0.320
Zip-NeRF [5]	0.172	0.270	0.181	0.281	0.212	0.217	0.251	0.279
Ours	0.115	0.219	0.137	0.233	0.188	0.172	0.175	0.258
Ours (16M)	0.123	0.245	0.150	0.244	0.206	0.192	0.196	0.322
Ours (8M)	0.145	0.262	0.169	0.274	0.288	0.274	0.239	0.394
Ours (pre-ex.)	0.291	0.370	0.396	0.375	0.381	0.333	0.358	0.508
SSIM↑ on Tanks and Temples [29]								
Method	Family	Francis	Horse	Lighthouse	M60	Panther	Playground	Train
Instant-NGP [36]	0.729	0.812	0.733	0.759	0.810	0.840	0.550	0.666
ADOP [43]	0.807	0.860	0.842	0.782	0.835	0.859	0.785	0.667
TRIPS [17]	0.849	0.879	0.871	0.792	0.862	0.884	0.771	0.768
3DGS [27]	0.871	0.901	0.889	0.834	0.901	0.910	0.834	0.791
Zip-NeRF [5]	0.893	0.918	0.909	0.835	0.905	0.908	0.846	0.813
Ours	0.903	0.913	0.912	0.822	0.903	0.916	0.870	0.783
Ours (16M)	0.902	0.903	0.909	0.814	0.898	0.909	0.859	0.733
Ours (8M)	0.894	0.897	0.905	0.801	0.853	0.881	0.831	0.697
Ours (pre-ex.)	0.758	0.801	0.768	0.754	0.780	0.801	0.717	0.597
PSNR↑ on Tanks and Temples [29]								
Method	Family	Francis	Horse	Lighthouse	M60	Panther	Playground	Train
Instant-NGP [36]	21.47	23.96	18.45	21.17	24.87	26.45	18.52	19.72
ADOP [43]	24.29	21.92	23.87	18.28	23.66	25.47	22.58	15.66
TRIPS [17]	24.03	20.06	23.45	18.09	25.52	27.73	24.10	18.79
3DGS [27]	25.05	27.64	24.18	21.76	27.82	28.35	25.65	21.69
Zip-NeRF [5]	28.05	29.55	27.67	22.31	28.86	28.84	26.62	22.10
Ours	28.24	26.36	27.05	20.08	27.52	29.03	24.69	19.33
Ours (16M)	28.25	26.03	26.58	19.78	27.10	28.67	24.11	17.89
Ours (8M)	28.06	26.16	26.78	19.56	25.03	27.17	23.78	17.51
Ours (pre-ex.)	15.35	15.71	14.26	15.4	15.95	16.32	16.25	14.44